*Figure S1. Zoomed-in XRD pattern of as-synthesized BaTiO$_3$, showing the split peak near 45 degrees which confirmed its tetragonal ferroelectric phase.*
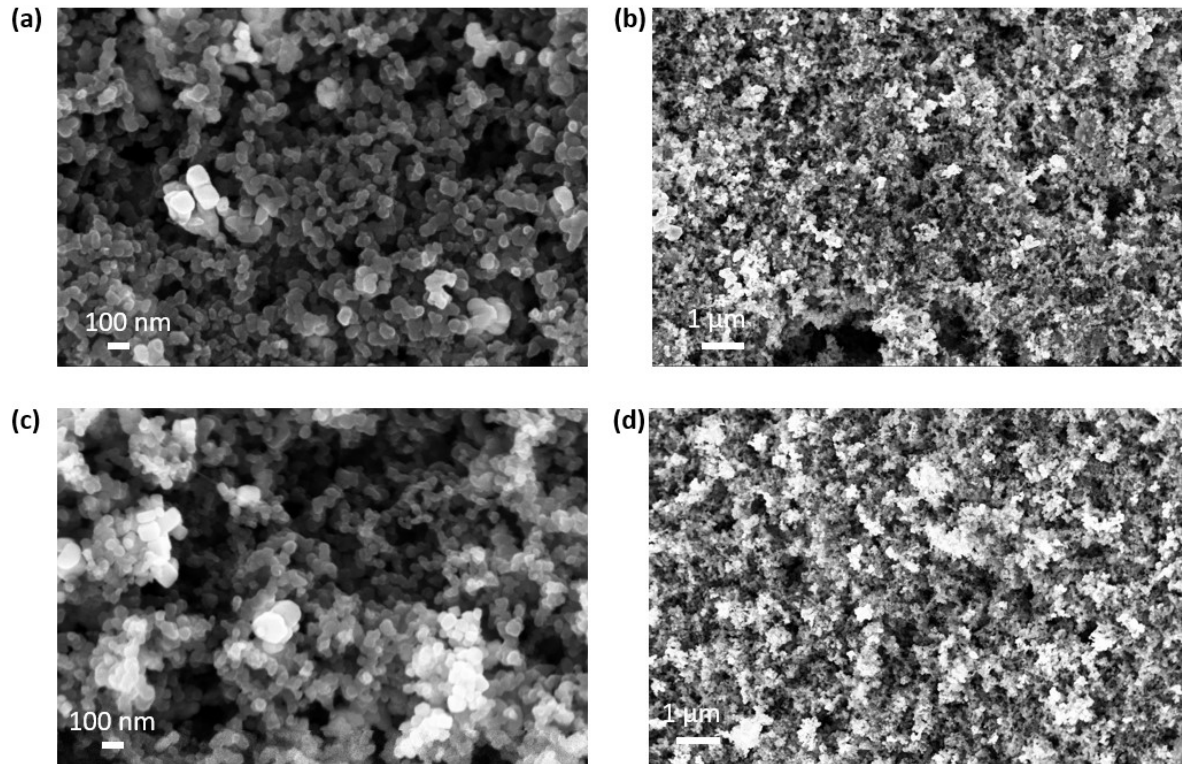
*Figure S2. (a)(b) SEM images of the BTO electrode, containing 45% as-synthesized BTO, 45% super P and 10% PVDF; (c)(d) SEM images of the STO electrode, containing 45% as-synthesized STO, 45% super P and 10% PVDF.*

**(a)**

Saw electrode

BTO electrode

Plate electrode

**(b)**

180.0 °

-180.0 °

HS PR Phase          80.0 nm

**(c)**

39.0 °

-39.5 °

HS PR Phase          600.0 nm

**(d)**

300    Potential (mV)    900

80 nm

**(e)**

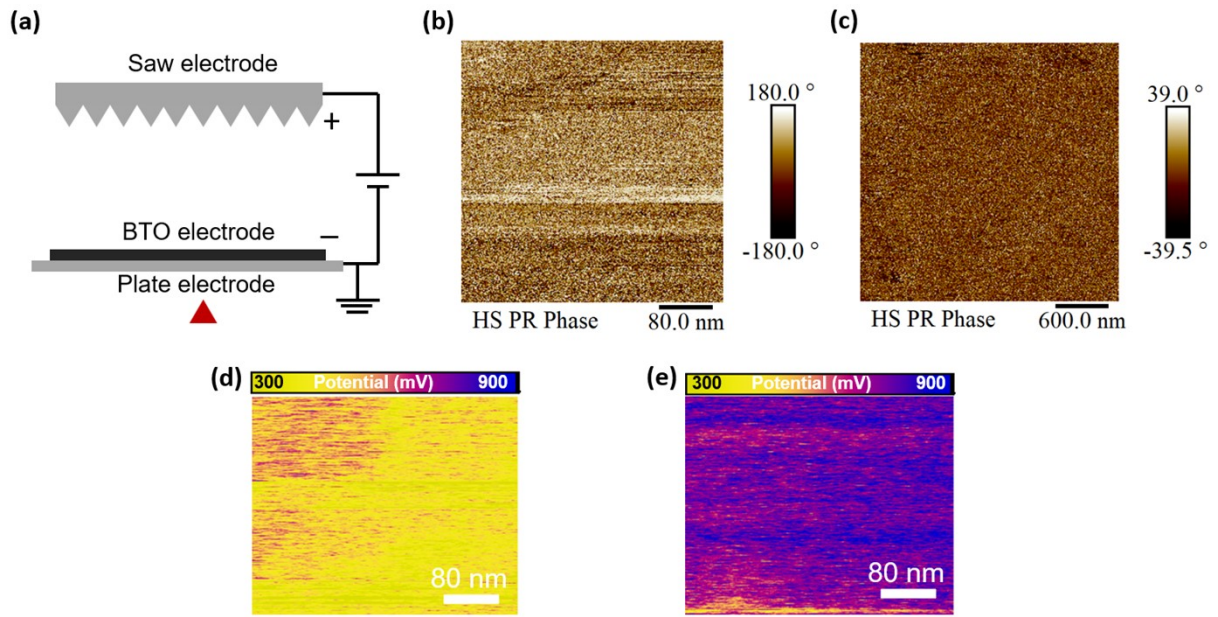300    Potential (mV)    900

80 nm

*Figure S3. (a) A schematic of the corona poling setup; PFM phase images of a (b) poled STO electrode and (c) unpoled STO electrode; KPFM surface potential images of the (d) unpoled BTO and (e) poled BTO electrodes.*
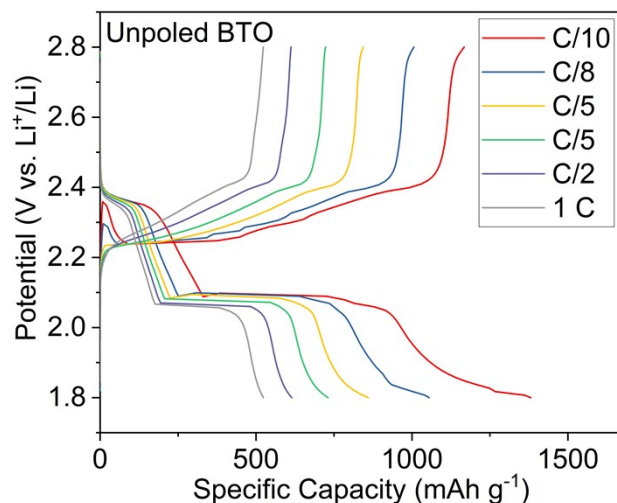
*Figure S4. Galvanostatic charge and discharge curves of the cell with an unpoled BTO cathode at C-rates between C/10 and 1 C.*
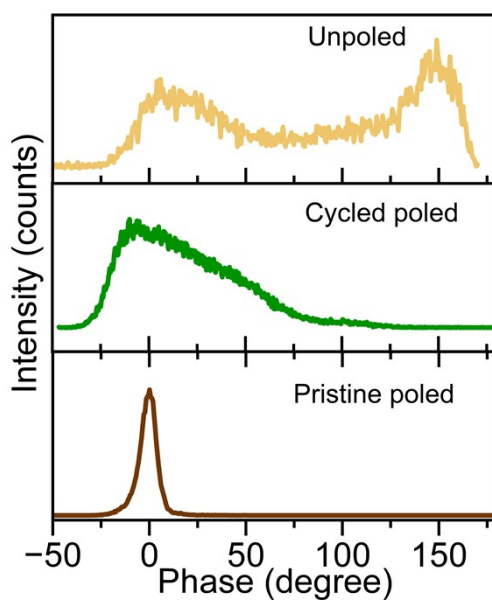


*Figure S5. The distribution of dipole orientations in the unpoled, cycled poled, and pristine poled BTO electrodes. The cycled poled electrode was cycled for 600 cycles at 1 C.*

(a)

Reflection kit
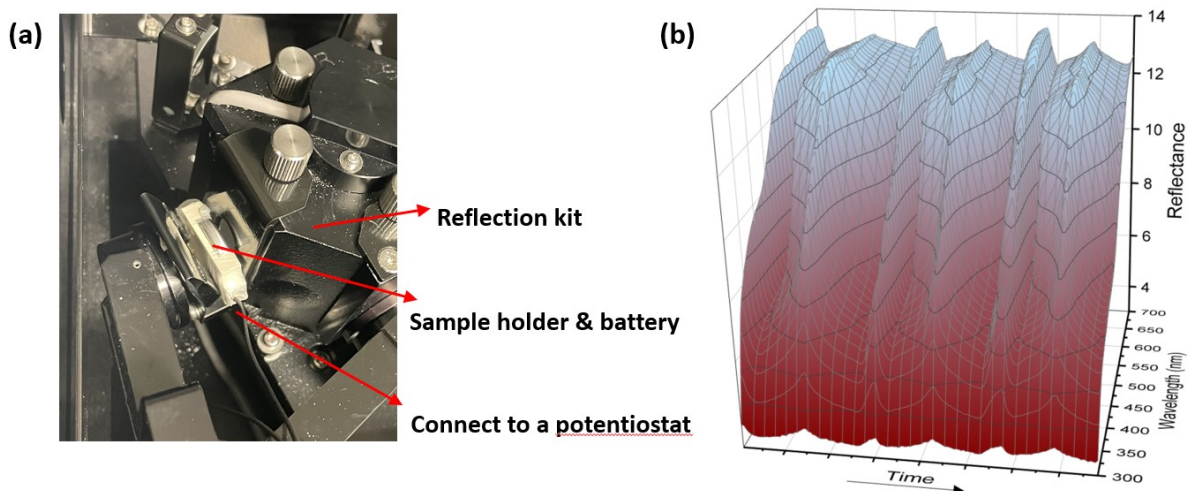
Sample holder & battery

Connect to a potentiostat

(b)

*Figure S6. (a) The setup for the operando UV-vis DRS measurements; (b) operando reflectance spectra collected over 3 galvanostatic cycles at C/6, of a cell with unpoled BTO.*
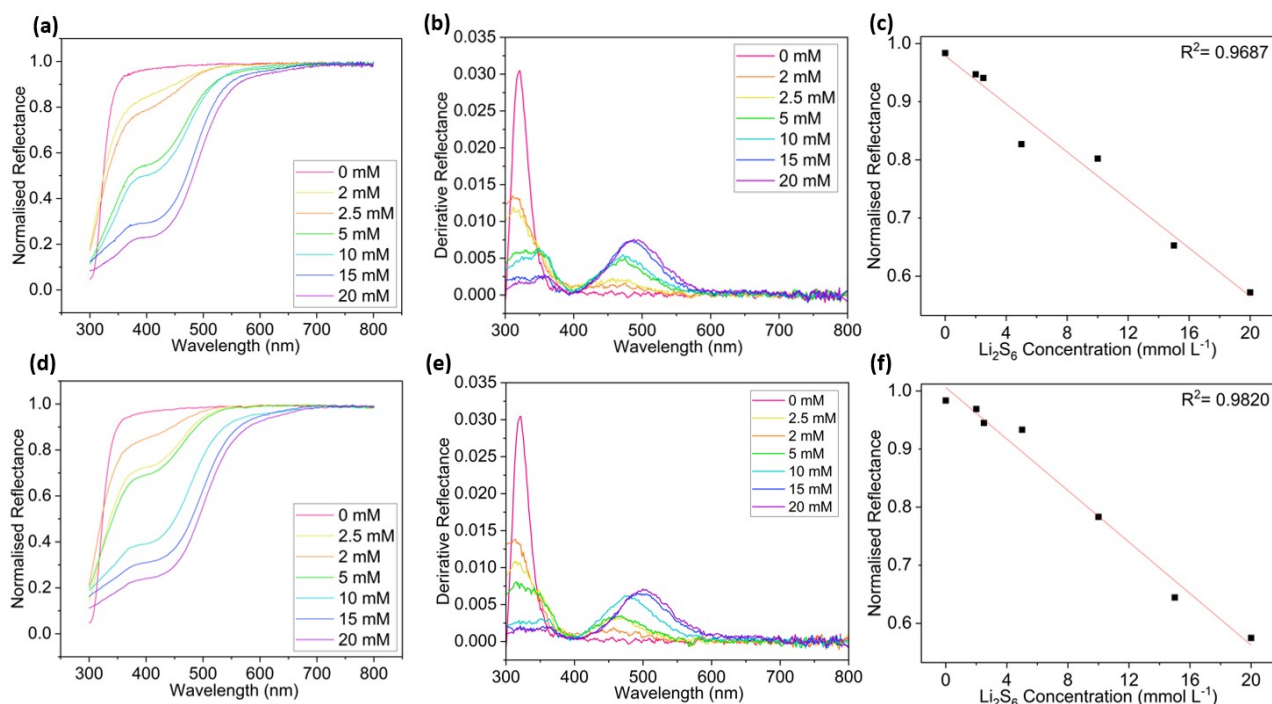
*Figure S7. UV-vis calibration measurements for $Li_2S_6$ and $Li_2S_8$. (a) UV-vis spectra of cells containing varying $Li_2S_6$ concentrations; and their (b) corresponding derivative spectra; (c) the linear fitting of the $Li_2S_6$ normalised reflectance and concentrations; (d) UV-vis spectra of cells containing varying $Li_2S_8$ concentrations; and their (e) corresponding derivative spectra; (f) the linear fitting of the $Li_2S_6$ normalised reflectance and concentrations.*

A series of calibration measurements was first conducted, using an *operando* coin cell without anode or cathode. A 0.5 mm spacer was added to the calibration cell to maintain the same pressure as a standard Li-S coin cell. Identical electrolytes were used, varying only the $Li_2S_6$ or $Li_2S_8$ concentrations between 0 and 20 mM, and the corresponding UV-vis spectra were collected (Figures S5(a) and S5(d)). A broad absorption at 400-550 nm was observed for both $Li_2S_6$ and $Li_2S_8$ that redshifted as the concentrations increased; this shift is more easily seen in the derivative spectra (Figure S5(b) and S5(e)). Following a method previously reported in the literature[1-3] (see experimental section for more details), and taking the range from the derivative maxima as 455-495 nm for $Li_2S_6$ and 463-507 nm for $Li_2S_8$, the wavelengths with the highest linear coefficient of determination ($R^2$) within these shift ranges were chosen as the specific wavelengths for $Li_2S_6$ or $Li_2S_8$. The highest $R^2$ values were obtained at 485 nm for

Li$_2$S$_6$ and 503 nm for Li$_2$S$_8$ (Figures S5(c) and S5(f)), which were therefore taken as the representative wavelengths for each species. The reflectance data from the *operando* UV-vis measurements were only converted into concentrations of Li$_2$S$_6$ and Li$_2$S$_8$ due to the low solubility of Li$_2$S$_4$ and Li$_2$S$_2$.
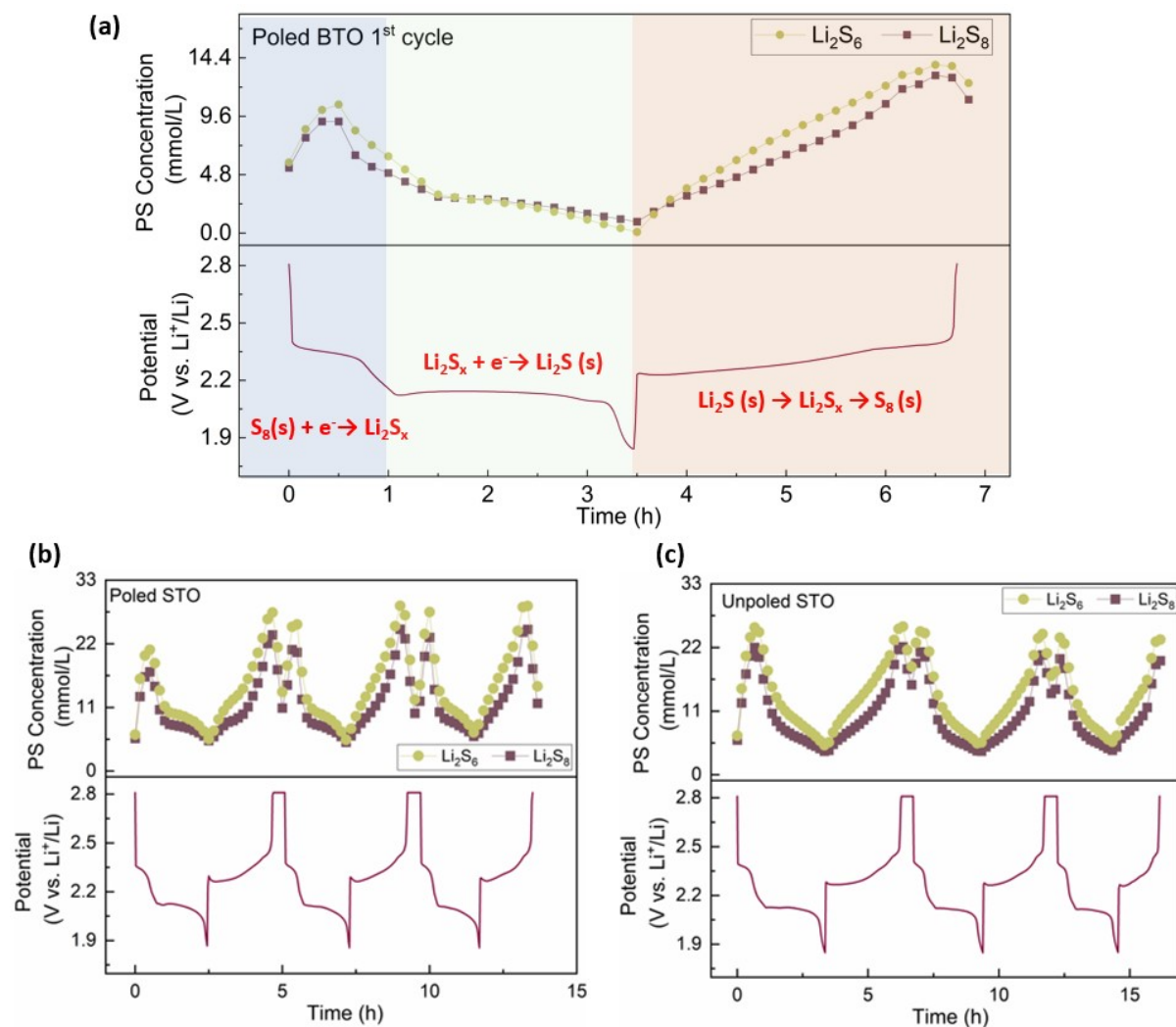


*Figure S8. (a) Variation in polysulfide concentration on the separator (top) with galvanostatic cycling (bottom), determined by UV-vis, of a cell containing the poled BTO electrode, highlighting the first discharge plateau (blue area), second discharge plateau (green area) and charge process (red area); the variation in polysulfide concentration on the separator (top) with galvanostatic cycling (bottom), determined by UV-vis, of cells containing the (d) poled STO and (e) unpoled STO electrodes.*
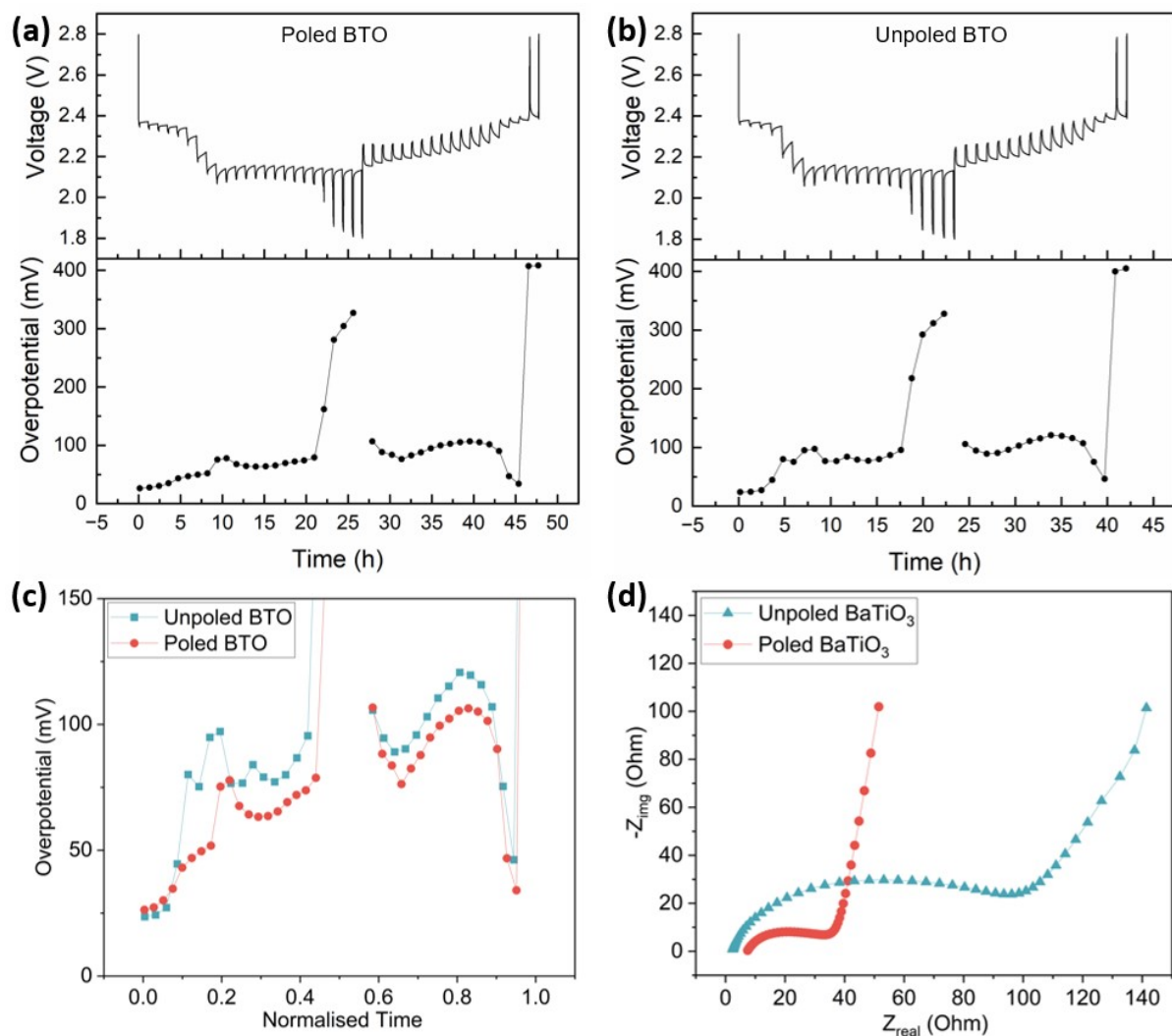
*Figure S9. GITT curves (top) of cells with the (a) poled BTO and (b) unpoled BTO electrodes, and their corresponding calculated cell overpotentials (bottom); (c) comparison of overpotentials of cells with the poled and unpoled BTO obtained from (a) and (b); (d) the Nyquist plots of cells containing poled and unpoled BTO electrodes at a fully-charged state after 1 cycle.*
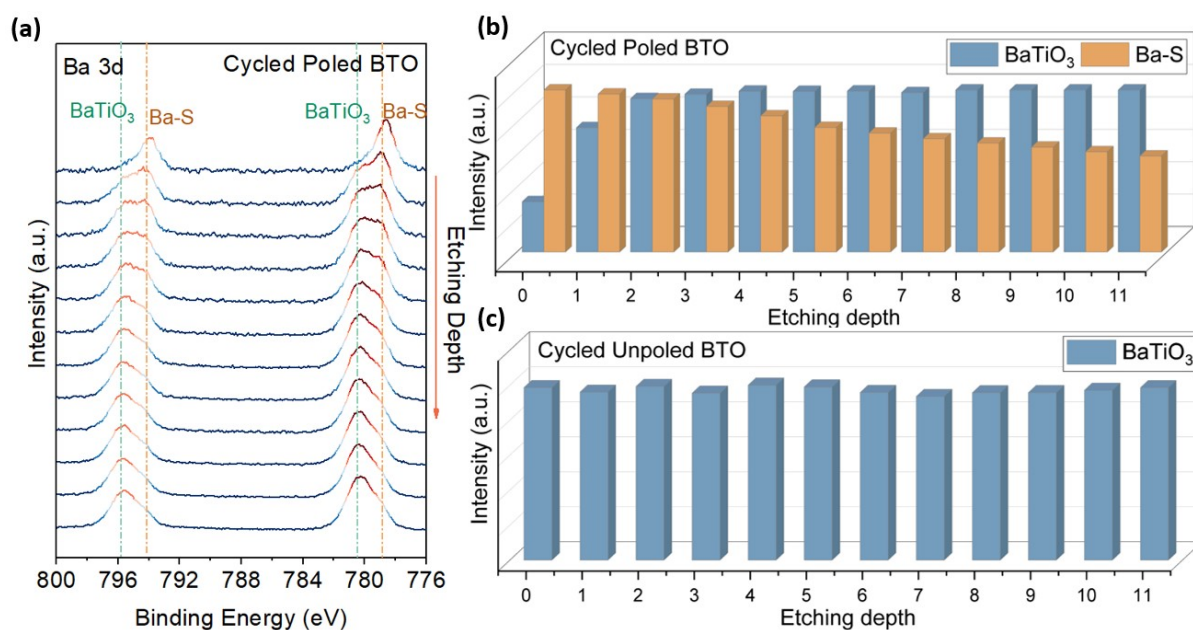
Figure S10. (a) Ba 3d XPS depth profile of the reverse-poled BTO electrode after 1 cycle at C/10; normalized peak intensities at each etching depth of (b) the cycled poled BTO and (c) cycled unpoled BTO electrodes.
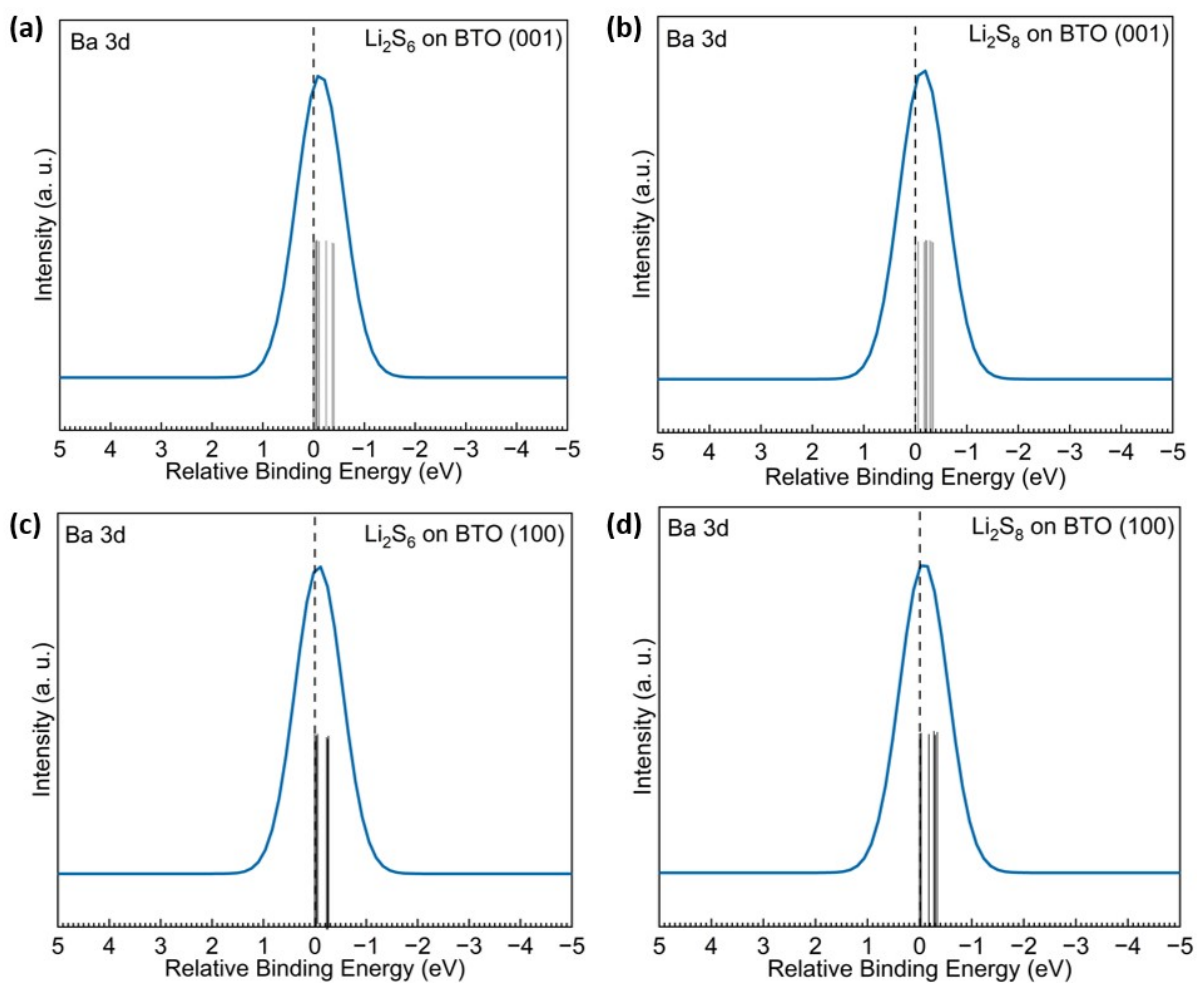
*Figure S11. The simulated Ba 3d shift of (a) $Li_2S_6$ on BTO (001), (b) $Li_2S_8$ on BTO (001), (c) $Li_2S_6$ on BTO (100) and (d) $Li_2S_8$ on BTO (100).*

*Table S1. Relative chemical shifts in the Ba 3d binding energies of $Li_2S_6$ and $Li_2S_8$ adsorbed on the BTO(001) surface. Values were obtained with the PBE functional with a Hubbard-type*

| Simulated Ba 3d | $Li_2S_6$ on BTO(001) (eV) | $Li_2S_8$ on BTO(001) (eV) | $Li_2S_6$ on BTO(100) (eV) | $Li_2S_8$ on BTO(100) (eV) |
|---|---|---|---|---|
| ΔBE (Ba1) | -0.11 | -0.06 | 0.00 | 0.00 |
| ΔBE (Ba2) | -0.08 | -0.20 | -0.04 | 0.00 |
| ΔBE (Ba3) | -0.06 | 0.00 | 0.00 | 0.00 |
| ΔBE (Ba4) | 0.00 | -0.22 | 0.00 | -0.01 |
| ΔBE (Ba5) | -0.24 | -0.17 | -0.24 | -0.29 |
| ΔBE (Ba6) | -0.24 | -0.31 | -0.27 | -0.33 |
| ΔBE (Ba7) | 0.00 | -0.06 | -0.02 | 0.00 |
| ΔBE (Ba8) | -0.37 | -0.29 | -0.22 | -0.30 |
| ΔBE (Ba9) | -0.40 | -0.35 | -0.22 | -0.19 |
| Average ΔBE | -0.17 | -0.18 | -0.11 | -0.12 |

*correction in the 3d states of Ti, where $U_{eff}$ = 2.6 eV. See Figure 6 for atom numbering.*

For the DFT models of the tetragonal phase BTO, the computed ground-state structural parameters are $a$ = 4.037 Å and $c$ = 4.101 Å, which are in excellent agreement with experimental values[4] $a_{exp}$ = 3.986 Å and $c_{exp}$ = 4.026 Å (deviations of +1.3% and +1.9%, respectively). The lattice tetragonality is therefore estimated as $c/a$ = 1.016 and the resulting ferroelectric structural distortion measured by the Ti off-center displacement is $\Delta_{Ti}$ = 0.011 (in units of the lattice constant $c$). The respective experimental distortion parameters are 1.010 and 0.015. The spontaneous polarization $P_s$ in $t$-BTO was calculated according to the Berry-phase approach.[5] We obtained a $P_s$ value of 26.2 $\mu C/cm^2$ within our PBE+$U$ scheme, which nicely reproduces the value reported in the experimental literature,[6] 26.0 $\mu C/cm^2$. For comparison, we have also performed standard PBE calculations to compute $P_s$ in $t$-BTO, which resulted in a value of 45.4 $\mu C/cm^2$. Our PBE result is very similar to that reported[7] where the

overestimation of $P_s$ in BTO as predicted by PBE is explained in terms of overestimations of both the polar distortion (from structural relaxation) and the Born effective charge (from the electronic structure minimization), which determine the polarization in ferroelectric materials.[8] Overestimation of both quantities is linked to the self-interaction error in DFT,[9,10] particularly problematic for semi-local functionals such as PBE. However, our calculations indicate that the inclusion of a Hubbard-type correction to the Ti 3d orbitals in BTO clearly improves the description of both quantities.

In our DFT simulations we considered the (001) surface to model a poled sample of BTO, whereas for modelling an unpoled system the (100) plane was chosen. Our assumption is justified by the fact that polarization normal to the surface is suppressed by depolarization fields.[11] Therefore, ferroelectric polarization should influence the polysulfide adsorption on the BTO(001) surface, but not the (100), which correspond to a modified and unmodified dipole alignment in the experiment setup, respectively. Both BTO surfaces can be seen as alternate packing planes of BaO and $TiO_2$ formulas, so a stoichiometric BTO slab representing either the (001) or the (100) plane exhibits one BaO surface and one $TiO_2$ surface. However, within the supercell approach it is desirable to build slabs with terminating surfaces that are symmetrically equivalent and can be mapped into each other by a mirror-type of symmetry operation in the middle of the slab, e.g., slabs with the same atomic layers at both terminating surfaces. This situation results in the creation of non-stoichiometric slabs. Fortunately, for II-IV perovskites like BTO, the BaO and $TiO_2$ layers are charge neutral; consequently, both surfaces are non-polar[12] and so their slab representation meets the condition required in periodic DFT calculations. Therefore, one can consider symmetric slabs to model the BTO (001) and (100) surfaces. We considered a BaO surface termination for both systems given that the chemical shifts obtained from Ba 3d XPS spectra suggest the formation of Ba-S bonds. Keeping these considerations in mind, we represented both surfaces with periodic slabs of five BaO layers and three $TiO_2$ layers, adding a vacuum gap of 15 Å in the $z$ axis to separate each slab from its periodic images. Laterally the supercells consist of (3 × 3) surface unit cells; therefore, the adsorption of one polysulfide molecule for every supercell corresponds to a surface coverage of 1/9 ML. This low coverage minimizes the lateral interactions and allows

us to focus on the role of ferroelectric distortion on the direct adsorbate-surface interactions. The polysulfide molecules were adsorbed on one face only and, together with the two topmost planes, were allowed to relax. The remaining planes were frozen at optimized bulk position such that ferroelectric effects are preserved through the simulations. All simulations included a dipole correction as implemented in VASP to compensate the asymmetry of the system.[13] Our modelling setup assumes that the molecular adsorption minimally affects the ferroelectric distortion parameters, which is reasonable considering the conditions of the experiments. Note that the geometries of adsorption found in the BTO(001) surface were tried on the BTO(100) surface; however, after geometry optimization, they converged to the configurations shown in Figure 6(b).

To evaluate the stability of the geometries of adsorption between the polysulfides and a given BTO surface, we estimated the adsorption energy $E_{ads}^{DFT}$ defined as:

$$E_{ads}^{DFT} = E_{slab + molecule} - (E_{slab} + E_{molecule})$$
(1)

where $E_{slab + molecule}$ is the total energy of the optimized substrate-adsorbate system, $E_{slab}$ corresponds to the total energy of the corresponding BTO surface, and $E_{molecule}$ refers to the total energy of the adsorbate in the gas phase at the lowest-energy configuration. Under this definition, a negative value of $E_{ads}^{DFT}$ indicates a stable adsorption complex.

Finally, for a direct comparison with XPS measurements, we performed core-level shift calculations in the so-called final state approximation.[14] Within this approach, the core-level shifts are estimated as total energy differences between two separate calculations.[15] This method neglects core-electron screening, but it does include the effect of screening by valence electrons. Note that this procedure does not yield correct absolute values for the core-level binding energies.[15] Consequently, one must consider core-level shifts $\Delta BE_{CL}(A)$ instead, which are defined as the difference in binding energy of specific core-electrons $BE_{CL}$ between an atom $A$ and a reference atom $A_{ref}$:

$$\Delta BE_{CL}(A) = BE_{CL}(A) - BE_{CL}(A_{ref}) \tag{2}$$

Our discussion focuses on the relative shifts of the Ba 3d levels of the Ba atoms at the surface. In our simulations, the reference Ba atom is the one yielding the lowest core-level binding energy in each case.

For the sake of simplicity, we only present the most stable adsorption complexes for each case, which are depicted in Figure 6. According to our DFT simulations, one of the Li atoms in $Li_2S_6$ and $Li_2S_8$ forms a bond with both BTO surfaces via an O atom, which is explained by the attraction of positively charged Li atoms in the polysulfide species with the negatively charged O atoms of the BTO surfaces. The adsorption complexes of $Li_2S_6$ and $Li_2S_8$ on BTO(001) feature Li-O bond lengths of 1.92 Å and 1.86 Å length, respectively. These bond lengths are considerably shorter on the BTO(100) surface, 1.76 Å for both cases, indicating a stronger attraction between Li in the adsorbate and the O atoms at this surface. However, the interaction between both polysulfides with the BTO(001) surface is also enhanced by the attraction between surface Ba and polysulfide S atoms, which is given by the number of Ba-S contact points. In the $Li_2S_6$-BTO(001) adsorption complex, three interacting S atoms of the adsorbate are atop sites (Ba6, Ba8 and Ba9 in Figure 6(b)), while one S is located on a bridge site (Ba5-Ba6); therefore, adsorbed $Li_2S_6$ is accommodated over four Ba surface atoms, with Ba-S interaction distances ranging between 3.24 Å and 3.60 Å. The $Li_2S_8$ on the BTO(001) surface occupies six Ba surface atoms: four S atoms are atop sites (Ba2, Ba6, Ba8 and Ba9), and one is on a bridge site (Ba4-Ba5). The Ba-S distance, within this system, ranges from 3.25 Å to 3.44 Å. In contrast, both the $Li_2S_6$- and $Li_2S_8$-BTO(100) adsorption complexes exhibit longer Ba-S distances: 3.57-3.66 Å and 3.50-3.55 Å, respectively. Hence, in terms of Ba-S interaction, both polysulfide molecules adsorb weakly on a BTO(100) surfaces, the Li-O bond being the main contributor to the adsorption energies of the complexes.

*References*

1       Xu, N. *et al.* Greatly suppressed shuttle effect for improved lithium sulfur battery performance through short chain intermediates. *Nano Lett.* **17**, 538-543 (2017).

2    Patel, M. U. *et al.* Li-S Battery Analyzed by UV/Vis in Operando Mode. *ChemSusChem* **6**, 1177-1181 (2013).

3    Liu, J. *et al.* Molecularly imprinted polymer enables high-efficiency recognition and trapping lithium polysulfides for stable lithium sulfur battery. *Nano Lett.* **17**, 5064-5070 (2017).

4    Shirane, G., Danner, H. & Pepinsky, R. Neutron diffraction study of orthorhombic BaTiO3. *Phys. Rev.* **105**, 856 (1957).

5    King-Smith, R. & Vanderbilt, D. Theory of polarization of crystalline solids. *Phys. Rev. B* **47**, 1651 (1993).

6    Wieder, H. Electrical behavior of barium titanatge single crystals at low temperatures. *Phys. Rev.* **99**, 1161 (1955).

7    Zhang, Y., Sun, J., Perdew, J. P. & Wu, X. Comparative first-principles studies of prototypical ferroelectric materials by LDA, GGA, and SCAN meta-GGA. *Phys. Rev. B* **96**, 035143 (2017).

8    Spaldin, N. A. A beginner's guide to the modern theory of polarization. *J. Solid State Chem.* **195**, 2-10 (2012).

9    Anisimov, V. I., Zaanen, J. & Andersen, O. K. Band theory and Mott insulators: Hubbard U instead of Stoner I. *Phys. Rev. B* **44**, 943 (1991).

10   Cohen, A. J., Mori-Sánchez, P. & Yang, W. Insights into current limitations of density functional theory. *Science* **321**, 792-794 (2008).

11   Zhong, W., King-Smith, R. & Vanderbilt, D. Giant LO-TO splittings in perovskite ferroelectrics. *Phys. Rev. Lett.* **72**, 3618 (1994).

12   Padilla, J. & Vanderbilt, D. Ab initio study of BaTiO3 surfaces. *Phys. Rev. B* **56**, 1625 (1997).

13   Makov, G. & Payne, M. C. Periodic boundary conditions in ab initio calculations. *Phys. Rev. B* **51**, 4014 (1995).

14   Birgersson, M., Almbladh, C.-O., Borg, M. & Andersen, J. N. Density-functional theory applied to Rh (111) and CO/Rh (111) systems: Geometries, energies, and chemical shifts. *Phys. Rev. B* **67**, 045402 (2003).

15   Köhler, L. & Kresse, G. Density functional study of CO on Rh (111). *Phys. Rev. B* **70**,

165405 (2004).